Tropical and Antarctic sea ice impacts of observed Southern Ocean warming and cooling trends since 1949

Xiyue Zhang[1] and Clara Deser[2]

[1]Department of Physics, University of Nevada, Reno, USA.

[2]National Center for Atmospheric Research, Boulder, USA.

Corresponding author: Xiyue Zhang (xiyuez@unr.edu)

Abstract

Southern Ocean (SO) sea surface temperatures (SSTs) warmed from approximately 1949–1978 and cooled slightly from 1979–2013. We compare the remote impacts of these SO trends using historical coupled model experiments in which the model's SO SST anomalies are nudged to observations. Compared to the control (no nudging) ensemble, the nudged ensemble shows enhanced SST warming in the tropical southeast Pacific and Atlantic, and greater Antarctic sea ice loss, during the SO warming period: analogous to the impacts of SO cooling but of opposite sign. The SO-driven response in the tropical Pacific (Atlantic) is statistically significant when considering the trend difference between the two periods, and accounts for 34% (59%) of the observed non-radiatively forced trend. Surface heat budget analysis indicates wind-evaporation-SST feedback dominates over shortwave cloud feedback in amplifying the SO-driven SST trends in the tropics during the SO warming period, opposite to that for the SO cooling period.

Introduction

Sea surface temperatures (SSTs) averaged over the Southern Ocean (SO) increased from the late 1940s to the late 1970s and decreased slightly thereafter, in contrast to the nearly monotonic rise in global-mean SSTs over the past seven decades (Figure 1a). These warming and cooling trends were accompanied by widespread opposite-signed changes in surface climate over the SO and coastal Antarctica as well as in Antarctic sea ice, providing physically-consistent independent evidence for their existence[1–3]. Whether the sign reversal of the SO and Antarctic trends reflects underlying naturally-occurring multidecadal variability as suggested by paleoclimate proxy

records and some coupled climate model simulations [4–6], or whether it is a part of the forced response to anthropogenic emissions is still under debate [2,7–10].

Regardless of its origin, the recent SO SST cooling trend from 1979 to 2013 has been shown to drive remote teleconnections to lower latitudes [11,12,9] and Antarctic sea ice expansion [11,13]. In particular, coupled model experiments reveal that the observed SO cooling induces significant cooling in the tropical eastern Pacific and Atlantic via the wind-evaporation-SST (WES) feedback mechanism, amplified by positive SST-low-cloud shortwave radiative feedbacks [11,9]. Idealized studies show an analogous response of the tropical eastern Pacific to Southern Hemisphere high-latitude cooling [14–16]. The teleconnection pathway from the SO in recent decades has significant implications for the role of the "pattern effect" [17,18] in estimated climate sensitivity. This is because the observed cooling in the tropical eastern Pacific opposes the expected weakening of the tropical Pacific zonal SST gradient induced by anthropogenic greenhouse gas emissions [19–21]. Furthermore, it remains unclear how much of the observed tropical SST trends that are not radiatively forced can be attributed to teleconnections from the SO.

While the low-latitude and Antarctic sea ice response to the recent SO SST cooling trend has been well studied [11,9], the impacts from the earlier SO SST warming phase have not yet been investigated. Here, we broaden the perspective on the role of the SO in tropical climate variability and Antarctic sea ice to include both the SO warming and cooling periods. Our experimental protocol follows that of Zhang et al.[11] and Kang et al. [9] in which SO SST anomalies in a global coupled model under historical radiative forcing are nudged to follow the observed SST anomaly evolution. This so-called "SO Pacemaker" ensemble is then compared with a control historical ensemble without nudging to identify the impact of observed SO SST

variability on the global climate system. If the mechanisms of the SO-induced teleconnections are robust and symmetric with respect to sign, we expect to find a warming of the tropical eastern Pacific and Atlantic, as well as reduced Antarctic sea ice, in response to observed SO warming during 1949–1978, in analogy with the cooling response during 1979–2013 identified previously. However, we note that the spatial pattern of SST trends within the SO differs somewhat between the SO cooling and warming phases, which may affect the magnitude of the tropical response[12]. For example, SO SST trend amplitudes are largest in the Pacific sector during the cooling phase (Figure 1c) and the Atlantic sector during the warming phase (Figure 1d).

We employ the Community Earth System Model (CESM) version 1 as in Zhang et al.[11], which is known to be deficient in its SST-low cloud feedback strength over the southeast Pacific [22,9]. Thus, our results should be viewed as a lower bound on the impact of SO multi-decadal SST variability on tropical Pacific climate since 1949. To amplify the signal of the SO-induced response, we also examine the difference between the simulated trends during the SO warming and cooling periods. This is particularly helpful for obtaining a statistically significant SO-driven response over the tropical Pacific where “noise” from internal variability associated with ENSO is large. Our study does not address the origin of the SO multi-decadal SST variability, which

may be influenced by teleconnections from the tropics. Rather, the objective of our study is to quantify the impact of SO SST variability on the tropics and Antarctic sea ice.

Results

Observed and simulated SST trends

The observed SST trends associated with the SO cooling and warming periods reveal somewhat distinctive spatial patterns, not only within the SO but throughout the global oceans (Figures 1c and 1d). In particular, the SO cooling period features a negative phase of the Pacific Decadal Oscillation (PDO) [23]/ Interdecadal Pacific Oscillation (IPO) [24], with cooling in the eastern tropical Pacific and a zonal dipole pattern of cooling in the east and warming in the west over North and South Pacific (Figure 1c). This period also features strong warming in the North Atlantic and weaker cooling in the South Atlantic, reminiscent of the positive phase of Atlantic Multidecadal Variability (AMV) [25]. On the other hand, the SO warming period is characterized by a hemispherically asymmetric pattern in both the Pacific and Atlantic sectors, with general cooling over much of the northern extratropics and warming in the southern extratropics (Figure 1d). The Pacific warming is concentrated in the southeast basin, in sharp contrast to the coherent SST trend patterns in the SO cooling period.

Although the global SST trend pattern during the SO warming period is not exactly opposite to that in the SO cooling period, many regions show trend reversals, including southeast Pacific (Figure 1b), equatorial eastern Pacific, as well as the North and South Atlantic (compare Figures 1c and 1d). Thus, it is not surprising that these regions also display prominent trend differences between the two periods (Figure 1e). In particular, the trend difference exhibits amplified cooling within the Atlantic and Pacific sectors of the SO, which extend into the tropical South Atlantic

and tropical southeast Pacific (Figure 1e). In addition, the Atlantic shows a strong interhemispheric SST gradient that resembles the positive phase of AMV, while the Pacific is characterized by a strong zonal gradient reminiscent of the negative phase of the PDO/IPO.

Next, we examine how much of the observed SST trend patterns can be explained by the radiatively-forced response, represented by the ensemble-mean of the CESM1 large ensemble ([LENS], where squared brackets denote ensemble-mean, Figures 1i–1k). The radiatively-forced response during the SO cooling period shows a typical global warming pattern with strong equatorial warming and muted warming in the tropical southeast Pacific (Figure 1i)[26]. On the other hand, the radiatively-forced response during the SO warming period shows pronounced hemispheric asymmetry with cooling across the Northern Hemisphere and warming in limited regions of the Southern Hemisphere including the tropical southeast Pacific and the Indian sector of the SO (Figure 1j). The [LENS] trend pattern during the SO warming period has been attributed to anthropogenic aerosol emissions over North America and Europe[27,28]. The difference in the radiatively-forced SST trends between the two periods is characterized by enhanced warming in the equatorial Pacific, the western Indian Ocean and the western North and South Pacific, with prominent cooling in the tropical southeast Pacific, the Sea of Okhotsk, and North Atlantic (Figure 1k). The Atlantic warms overall and has slightly stronger warming to the north than the south (Figure 1k).

When the impact of observed SO SST variability is added to the radiatively-forced response, given by the SOPACE ensemble-mean [SOPACE], the simulated SST trend pattern shows greater similarity to observations for both periods (Figure 1f-h). In the SO warming period, the SST trend pattern correlation for 40°S to 40°N between [LENS] and observations is 0.42, while that between [SOPACE] and observations is 0.55. In the SO cooling period, although the pattern

correlations are generally lower, we still find a higher correlation between observations and [SOPACE] (0.25) than with [LENS] (0.15).

We can isolate the SO-driven response by subtracting the radiatively-forced response from [SOPACE] (e.g., SO-driven = [SOPACE] – [LENS], Figures 1l–1n). As shown in Zhang et al.[11], SO cooling induces a significant cooling in the tropical South Atlantic but only has a weak impact on the tropical Pacific (Figure 1l). SO warming, on the other hand, leads to significant warming in the tropical South Atlantic and a broad warming (albeit not statistically significant) in the tropical Pacific that reaches the Maritime Continent (Figure 1m). Furthermore, the North Pacific shows a positive PDO pattern in the SO warming period. This could result from the more extensive tropical Pacific warming that reaches the central Pacific, driving an atmospheric teleconnection to the North Pacific which then produces a PDO-like SST response. The stronger SO-driven teleconnection in the SO warming period may result from the more equatorward location of the positive SST trend in the Pacific sector of the SO (Figure 1d).

Although the tropical Pacific response is not statistically significant in either period, the trend difference between the two periods is significant in the equatorial and tropical southeast Pacific (Figure 1n). This is an important result: it suggests that stronger forcing from the SO (obtained here by calculating the trend difference) can result in a statistically significant (at 95% confidence level) response in the tropical Pacific even in a model with deficient SST–low cloud feedback strength[22,9]. Unlike the tropical Pacific, the SO-driven response in the tropical South Atlantic is statistically significant in both periods and in the trend difference. The weaker internal

variability in the tropical Atlantic[29] compared to the tropical Pacific could explain the higher level of statistical significance of the SO-driven response.

To further quantify the SO-driven response in the tropics and to consider it in the context of internal variability, we average the SST trends within the tropical southeast Pacific and South Atlantic (regions highlighted in Figure 1c-e) for each ensemble member of SOPACE and LENS (Figure 2a and 2b). In the tropical southeast Pacific, the SOPACE distribution is shifted slightly towards the observed value compared to the LENS distribution in both periods, although there is considerable spread across members due to internal variability (Figure 2a). When we consider the trend difference between the two periods, while the observed value would be an outlier in LENS, it is no longer an outlier in SOPACE. This suggests that the inclusion of observed SO SST variability increases the likelihood that CESM1 can simulate the magnitude of the observed SST trend difference in the tropical southeast Pacific.

A more prominent impact of SO SST variability is found in the tropical South Atlantic. As pointed out by Zhang et al. [11], SO cooling induces significant cooling in the tropical South Atlantic, making the SOPACE ensemble distinct from the LENS ensemble (Figure 2b). The observed SST trend lies within the middle 50th percentile of the SOPACE distribution. As for the SO warming period, although the observed SST trend is outside of the range of both SOPACE and LENS distributions, the SOPACE ensemble is significantly warmer and closer to the observed trend than the LENS ensemble. The trend difference between the two periods in this region is characterized by two contrasting ensembles: all LENS members show positive values,

while nearly half of SOPACE members show negative values consistent with the sign in observations.

Next, we quantitatively assess SO's contribution to observed SST trends in the tropical southeast Pacific and South Atlantic. Because there is little resemblance between the SO SST trends in observations and those simulated in [LENS], we conclude that SO warming and cooling are not a radiatively forced response in CESM1. We then subtract the radiatively-forced response [LENS] from observations to represent the observed SST trends that are not radiatively forced in the tropical southeast Pacific and South Atlantic (black bars on Figures 2d and 2e). A part of this unforced SST trend can be attributed to the SO, which is represented by the SO-driven response ([SOPACE] – [LENS], green hatched bars on Figures 2d and 2e). For both periods in both basins, the SO-driven response has the same sign as the observed unforced SST trends (Figures 2d and 2e).

In the tropical southeast Pacific, the SO-driven response explains 19% of the observed unforced SST trend in the SO cooling period. This is in sharp contrast to the SO warming period, where the SO-driven response explains 113% of the observed unforced warming. This suggests that other modes of variability act to cool the tropical southeast Pacific during this period. When we combine the two periods, 34% of the observed unforced SST trend difference can be explained by the SO (Figure 2d). The tropical South Atlantic shows an even larger contribution from the SO (Figure 2e). In this region, the SO-driven response accounts for 85% of the observed unforced cooling, 47% of the observed unforced warming, and 59% of the observed unforced

trend difference. These results point to a major role for the SO in driving multi-decadal SST trends in the tropical southeast Pacific and South Atlantic.

Surface mixed-layer heat budget analysis

Kim et al.[22] probed the mechanisms for the SO-driven equatorward teleconnection using idealized coupled model experiments in which the zonal-mean solar insolation over the SH extratropics (45º–65ºS) is abruptly reduced by 0.8 PW (equivalent to 1.6 W/m^2 in the global mean). They found that the dominant mechanism for the transient SST response involves an initial northward advection of the high-latitude SST anomalies into the subtropics via the climatological winds on a time scale of a few years, followed by amplification within the subtropical southeast Pacific via the wind-evaporation-SST feedback, coastal upwelling, and subtropical low-cloud feedback.

While it is difficult to analyze the transient adjustment pathways in our time-evolving SOPACE simulations, we can quantify how processes suggested by Kim et al.[22] contribute to the SO-driven SST response in the tropics by diagnosing the upper ocean mixed-layer heat budget [26,30,14] following the procedure in Zhang et al. [11]. Briefly, the mixed-layer heat storage is determined by net surface shortwave and longwave fluxes, sensible and latent heat fluxes, and heat flux due to ocean dynamics. The dependency of latent heat flux on SST (Newtonian cooling) enables us to

diagnose SST trend (denoted by superscript $\boldsymbol{t}$) based on trends of radiative and turbulent heat flux terms:

$$\boldsymbol{T_s^t = -\frac{1}{\alpha \overline{LH}}(F_{SW}^t + F_{LW}^t + SH^t + F_O^t + LH_W^t + LH_{RH}^t + LH_{\Delta T}^t)} \qquad (1)$$

Here, $\boldsymbol{T_s}$ is SST, $\boldsymbol{\alpha = \frac{L_v}{R_v T^2} \approx 0.06}$ K^{-1}, $\boldsymbol{LH}$ is latent heat flux (overbar denotes climatology), $\boldsymbol{F_{SW}}$ is shortwave flux, $\boldsymbol{F_{LW}}$ is longwave flux, $\boldsymbol{SH}$ is sensible heat flux, and $\boldsymbol{F_O}$ is heat flux due to ocean dynamics. The latent heat flux $\boldsymbol{LH}$ is decomposed into atmospheric forcing due to changes in near-surface wind speed ($\boldsymbol{LH_W}$), near-surface relative humidity ($\boldsymbol{LH_{RH}}$), and air-sea temperature difference ($\boldsymbol{LH_{\Delta T}}$, see Methods for more details).

We analyze the surface heat budgets for SST trends during the SO cooling and warming periods, as well as the difference in trends between the two periods. First, we compare the SO-driven SST trends from [SOPACE] – [LENS] (Figure 3a-c) with those estimated from equation (1) (Figure 3d-f). The general cooling and warming patterns in the tropical oceans are qualitatively captured by the net surface heat budget calculation, but their amplitudes are overestimated especially in the cooling period. In the SO warming period, the heat budget quantitatively captures the equatorial warming trend maxima in all three ocean basins, the meridional dipole in the Atlantic, and the zonal gradients in the Indian Ocean and North Pacific (Figure 3e). However, in the SO cooling period, the heat budget overestimates the equatorial cooling maxima (Figure 3d), which results in exaggerated tropical cooling in the difference between the two cooling and warming periods (Figure 3f). This overestimation may be due to nonlinear interactions between the LH

terms, or errors in estimating the air-sea temperature difference due to the extrapolated 2-m air temperature.

Among the terms in equation (1), the shortwave flux $\boldsymbol{F_{SW}^{t}}$, latent heat flux $\boldsymbol{LH^{t}}$, and ocean dynamics $\boldsymbol{F_{O}^{t}}$ have the most prominent contributions to the SST trends in both periods ($\boldsymbol{LW^{t}}$and $\boldsymbol{SH^{t}}$ are small, Figure S1). We will focus our discussion on $\boldsymbol{F_{SW}^{t}}$ and $\boldsymbol{LH^{t}}$, as $\boldsymbol{F_{O}^{t}}$ is computed as a residual term and harder to interpret physically.

- $\boldsymbol{F_{SW}^{t}}$: As highlighted in Zhang et al. [11], the shortwave flux plays a dominant role in the SST cooling off the west coasts of South America and Africa (Figure 3g). This is due to the local positive low-cloud feedback that contributes to SO-driven cooling [22,9]. Indeed, we find high spatial correlation between the responses of cloud liquid water path and shortwave cloud radiative effect (which dominates the net shortwave flux, Figure S2). Interestingly, we also find shortwave cooling (and a corresponding increase of liquid water path) off the coast of Chile that extends to the northwest during the SO warming period (Figure 3h). This may seem counterintuitive, as subtropical low cloud fraction is expected to decrease with SST warming [31], which is the case in the subtropical Atlantic. However, other factors such as estimated inversion strength or horizontal temperature advection can also affect low clouds in the subtropical Pacific [32].

- $\boldsymbol{LH^{t}}$: In the SO cooling period, $\boldsymbol{LH^{t}_{W}}$ dominates the equatorial Atlantic via southeasterly surface wind anomalies (Figure 3j). In the tropical Pacific, $\boldsymbol{LH^{t}_{W}}$ contributes to cooling in the northeast and near the South Pacific convergence zone. In the SO warming period, $\boldsymbol{LH^{t}_{W}}$ is the main contributor of the SST warming in the tropical Pacific and Atlantic via northwesterly surface wind anomalies (Figure 3k). The difference between the two periods is

dominated by $\boldsymbol{LH^t_W}$, suggesting strong wind-induced latent heat cooling in the equatorial Atlantic and Pacific driven by SO cooling (Figure 3l). The contributions from $\boldsymbol{LH^t_{RH}}$ and $\boldsymbol{LH^t_{\Delta T}}$ are not consistently robust in both periods comparing to $\boldsymbol{LH^t_W}$, although locally they can be important (Figure S1).

To summarize, while shortwave cloud feedback plays a major role in amplifying the SO-driven cooling in the tropical southeast Pacific and South Atlantic, this is not the case for the SO warming period. Wind-induced latent heat flux, hence the wind-evaporation-SST feedback, dominates the SO-driven surface heat budget during the SO warming period.

Antarctic sea ice response

We compare the simulated Antarctic sea ice concentration trends for the SO warming and cooling periods, with and without the influence of observed SO SST variability. Antarctic sea ice concentration trends in the SO cooling and warming periods in [SOPACE] share some similar features, with a pattern correlation of 0.73 (Figures 4b and 4c). For example, there is significant sea ice loss in the Weddell Sea and the Indian sector north of 60°S, while south of 60°S in the Indian sector the sea ice fraction trend is positive. However, the contribution from radiative forcing differs in the two periods: in the SO cooling period, [LENS] shows ice loss nearly everywhere (Figure 4e), while in the SO warming period, the [LENS] sea ice trends are weaker and less homogeneous (Figure 4f). The trend difference between the two periods shows a nearly opposite pattern for [SOPACE] and [LENS] (Figure 4d and 4g), suggesting that the SO-driven response tends to oppose the radiatively-forced sea ice loss.

Indeed, the SO-driven sea ice response is opposite to [LENS] in both periods (Figure 4h and 4i). The pattern correlation between SO-driven and [LENS] sea ice trends is -0.63 for the SO cooling

period and -0.30 for the SO warming period. Furthermore, the sea ice trend differences between the two periods are almost exactly opposite between SO-driven and [LENS], with a pattern correlation of -0.85. This further highlights the opposing effect of radiative forcing (which leads to ice loss) and SO SST cooling (which leads to ice gain) on Antarctic sea ice trends.

The inclusion of observed SO SST variability also affects individual ensemble members by narrowing the ensemble range of total Antarctic sea ice extent (SIE) trends (Figure 2c). For the SO cooling period, all LENS members show negative SIE trends, while a few SOPACE members show positive SIE trends that are consistent in sign with the observed trend, albeit weaker in magnitude. SO-driven sea ice gain can explain 54% of the observed unforced SIE trend during the SO cooling period (Figure 2f). For the SO warming period, a few LENS members show positive SIE trends while all SOPACE members show negative SIE trends. Although there are no passive-microwave satellite measurements of Antarctic sea ice before 1979, visual satellite imagery beginning in 1973 suggests there was a marked decrease in SIE from 1973-1979[1]. Reconstructed Antarctic SIE suggests a weak negative trend during the SO warming period; this trend lies near the middle of the LENS distribution and at the upper end of the SOPACE distribution (Figure 2c). Overall, SOPACE members show more sea ice loss during the SO warming period than LENS members, though the range of SOPACE lies fully within the range of LENS (Figure 2c). The trend difference between the two periods, however, shows ice loss in nearly all LENS members but ice gain in nearly all SOPACE members. Thus, in the trend difference, observed SO cooling more than offsets the radiatively forced response, leading to a net gain in Antarctic sea ice in nearly all ensemble members of SOPACE. Only the SOPACE ensemble can capture the positive reconstructed Antarctic SIE trend difference. While the SO-driven Antarctic sea ice response explains more than 50% of the observed and reconstructed

unforced Antarctic SIE trend during the SO cooling period, its contribution in the SO warming period is much weaker. The SIE trend difference is dominated by the SO cooling period, where SO-driven response explains 77% of the reconstructed Antarctic SIE trend difference (Figure 2f).

Discussion

We have broadened the perspective on the role of the SO in recent tropical climate trends by introducing a SO Pacemaker ensemble for the period of SO warming (1949-1978) using the same protocol as Zhang et al. [10]. Combined with Zhang et al.'s SOPACE experiments for the SO cooling period (1979-2013), this new ensemble allows us to assess the robustness of the mechanisms of the SO induced teleconnections and whether they are symmetric with respect to the sign of the SO SST trends. It also allows us to strengthen the signal of the SO-induced response by computing the difference in trends between the SO cooling and warming periods. We find that the SO-driven response in the tropical southeast Pacific is statistically significant when we consider the trend difference between the two periods and accounts for 34% of the observed unforced trend difference. In the tropical South Atlantic, the SO-driven response explains 59% of the observed SST trend difference that is not radiatively-forced. In both the tropical southeast Pacific and South Atlantic, SO-driven cooling offsets radiatively-forced warming in the observed SST trend difference. The inclusion of SO SST variability allows the model ensemble to better capture the observed tropical SST trends and Antarctic sea ice trends, as well as reconstructed Antarctic SIE trends before 1979.

With our existing experiments, we cannot isolate the relative roles of the Atlantic and Pacific sectors of the SO on influencing the tropical oceans. However, we find that during the SO warming period, the Atlantic sector of the SO warmed nearly twice as much as the Pacific sector

298 of the SO, with a similar ratio of SO-induced warming between the tropical South Atlantic and
299 southeast Pacific. But during the SO cooling period, the Pacific sector of the SO cooled more
300 than the Atlantic sector, yet the SO-driven cooling in the tropical southeast Pacific was less than
301 the cooling in the tropical South Atlantic. This contrasts with the results of Dong et al. [12] who
302 used slab-ocean experiment with prescribed q-flux cooling in the eastern Pacific and Atlantic
303 sectors of the SO separately. They found that for the same magnitude of cooling, the eastern
304 Pacific sector of the SO drives in stronger cooling response in the equatorial eastern Pacific
305 compared to the Atlantic sector of the SO. Further coupled model experiments are needed to
306 investigate the regional impacts of SST variability from different sectors of the SO.

307 While we have confirmed that by differencing the SO warming and cooling periods, the SO-
308 driven tropical Pacific response becomes stronger, we also acknowledge that the magnitude of
309 this response is sensitive to the strength of the shortwave cloud feedback [15]. Contrary to previous
310 studies that highlight a prominent role of the shortwave low cloud feedback [22], here we find a
311 weaker contribution from the shortwave flux in the SO warming period. This is not surprising,
312 given that the shortwave cloud feedback in CESM1 is known to be weaker than observed [22,9].
313 Given this sensitivity, it would be immensely valuable to conduct long historical SO Pacemaker
314 experiments with other coupled models. Additionally, the role of mean state biases in the
315 strength and pattern of the SO-driven response warrants future investigation with targeted
316 numerical experiments.

317 A major implication of the tropical warming induced by observed SO warming is that future SO
318 warming may also contribute to tropical Pacific and Atlantic warming. Because the SO SST
319 warming is delayed due to SO heat uptake[2], on centennial time scales it could contribute further
320 to the projected tropical warming. On the other hand, modeling evidence suggests that enhanced

melting from Antarctic Ice Sheet can lead to SO cooling that further influences tropical SST [33–35]. The relative balance and time scales of the two processes will affect the SO's ongoing contribution to the projected evolution of tropical Pacific and Atlantic SSTs.

Methods

CESM1 pacemaker simulations

The original "SO Pacemaker" (SOPACE) simulations include a 20-member ensemble for the period 1975–2013 using CESM1 **[11]**. Here, we use the same model and experimental protocol, but for the earlier period 1945–1978. Briefly, we conduct a 20 member ensemble of SOPACE simulations with the global fully-coupled CESM version 1.1.2 at 1º horizontal resolution under historical radiative forcing. For each member, the model's SST anomalies (e.g., deviations from the model's seasonally-varying climatology) are nudged to the observed SST anomaly evolution south of 40ºS with a linear buffer zone at 35–40ºS. For consistency, we use observed SSTs from the NOAA Extended Reconstruction Sea Surface Temperature version 3b (ERSSTv3b) data set on a 2º grid**[36]**. All 20 SOPACE members are initialized from the first member of the 40-member CESM1 Large Ensemble (LENS)**[37]** on 1 Jan 1920, with a random initial atmospheric temperature perturbation of $O(10^{-14})$ K to create ensemble spread. The first 4 years of the simulations are considered as spin-up and excluded from trend calculations. The ensemble mean of LENS, denoted [LENS], represents the model's radiatively-forced response, and the ensemble mean of SOPACE, denoted [SOPACE], represents the model's radiatively-forced response plus the

response to observed SO SST variability. The difference between [SOPACE] and [LENS], which we call the SO-drive response, isolates the influence of observed SO SST variability.

Statistical methods

Linear trends over the early SO warming period (1949–1978) and the late SO cooling period (1979–2013) are calculated from annual averages of monthly anomalies for observations, Antarctic SIE reconstruction, and both the ensemble–mean and individual members of LENS and SOPACE. We also calculate the difference in trends between the SO cooling and warming periods, where the trends in each period are expressed in units of decade^{-1} in order to compare their rates of change. The observed and ensemble-mean trend significance for either the SO cooling or warming period is assessed using the two-sided student's t-test adjusted for autocorrelation[38,39] at 95% confidence level. The statistical significance of the difference between the trends for the SO warming and SO cooling periods in observations is assessed by comparing the adjusted 95% confidence intervals of trends estimated with the two-sided student's *t* distribution[38]. Regions without overlapping trend intervals are interpreted as having statistically significant trend differences. For simulations, the significance of the trend difference between two periods is assessed by comparing whether the ensemble-mean of each period is different relative to the ensemble spread of the trends in each period using a two-sided student's t-test at 95% confidence interval.

Observational data

We compare the model's simulated SST trends with the ERSSTv3b data set at 2° global resolution (i.e., the same data set used for the Pacemaker ensemble), and the model's simulated Antarctic sea ice concentration trends with the passive-microwave NASA Goddard Bootstrap

version 2 sea ice product on a 25 km x 25 km grid [40], which begins in 1979. We also use the reconstructed Antarctic sea ice extent [3] to compare the model's simulated Antarctic sea ice extent trend for both periods.

Mixed-layer budget

In equation (1), the trend of heat storage on the left hand side is negligible[11]. This allows us to compute the heat flux due to ocean dynamics as a residual term. To diagnose the SST trends with equation (1), we start with the approximated surface latent heat flux formula $\boldsymbol{LH} = -\boldsymbol{L_v c_E \rho_a W}(\mathbf{1} - \boldsymbol{RH_0 e^{\alpha \Delta T}})\boldsymbol{q_s}(\boldsymbol{T_s})$, where $\boldsymbol{L_v}$ is the latent heat of vaporization, $\boldsymbol{c_E}$ is the transfer coefficient, $\boldsymbol{W}$ is the wind speed at 10 m, $\boldsymbol{RH_0}$ is the relative humidity at the lowest atmospheric model level, $\boldsymbol{\alpha} = \frac{\boldsymbol{L_v}}{\boldsymbol{R_v T^2}} \approx \mathbf{0.06}$ K^{-1}, $\boldsymbol{\Delta T} = \boldsymbol{T_a} - \boldsymbol{T_s}$ is the air-sea temperature difference, $\boldsymbol{T_a}$ is air temperature at 2 m, $\boldsymbol{T_s}$ is SST, and $\boldsymbol{q_s}$ is the saturation specific

humidity. We can linearize the latent heat flux trend (superscript $\boldsymbol{t}$) as $\boldsymbol{LH^t = \frac{\partial LH}{\partial T_s} T_s^t +}$ $\boldsymbol{\frac{\partial LH}{\partial W} W^t + \frac{\partial LH}{\partial RH_0} RH_0^t + \frac{\partial LH}{\partial \Delta T} \Delta T^t}$. The last 3 right-hand-side terms are defined as

$$\boldsymbol{LH_W^t = \frac{\partial LH}{\partial W} W^t = \overline{LH} \frac{W^t}{\overline{W}},} \quad (2)$$

$$\boldsymbol{LH_{RH}^t = \frac{\partial LH}{\partial RH_0} RH_0^t = -\frac{\overline{LH} RH_0^t}{e^{-\alpha \overline{\Delta T}} - \overline{RH_0}},} \quad (3)$$

$$\boldsymbol{LH_{\Delta T}^t = \frac{\partial LH}{\partial \Delta T} \Delta T^t = -\frac{\alpha \overline{LH}\, \overline{RH_0} \Delta T^t}{e^{-\alpha \overline{\Delta T}} - \overline{RH_0}},} \quad (4)$$

while the first term of the right-hand-side is the SST damping term $\boldsymbol{\frac{\partial LH}{\partial T_s} T_s^t = \alpha \overline{LH}\, T_s^t}$. Figures 3 and S1 show the SST contributions from these terms normalized by $\boldsymbol{-\alpha \overline{LH}}$.

Data availability

The full CESM1 LENS dataset is available from NCAR's Climate Data Gateway at https://www.earthsystemgrid.org/dataset/ucar.cgd.ccsm4.cesmLE.html. The ERSSTv3b data are available at NOAA Physical Sciences Laboratory https://psl.noaa.gov/data/gridded/data.noaa.ersst.v3.html. The sea ice data are available at the National Snow and Ice Data Center. The satellite sea ice data are available at https://nsidc.org/data/nsidc-0079/. The reconstructed Antarctic sea ice extent data are available at https://doi.org/10.7265/55x7-we68. The CESM1 SOPACE dataset is available upon request from the corresponding author.

Code availability

The Python code used to generate manuscript figures is available upon request from the corresponding author.

Acknowledgments

We thank the editor and two anonymous reviewers for their constructive comments that have improved the article. This study was partially supported by the Advanced Study Program postdoctoral fellowship from the National Center for Atmospheric Research (NCAR) and the National Science Foundation (NSF) Office of Polar Programs. The materials are based upon work supported by NCAR, which is a major facility sponsored by the NSF under cooperative agreement 1852977. The authors would like to acknowledge high-performance computing support from Cheyenne provided by NCAR's Computational and Information Systems Laboratory, sponsored by the NSF.

Competing interests

The authors declare no Competing Financial or Non-Financial Interests.

Author contributions

Both authors designed the research, discussed the results, and wrote the manuscript. X. Z. carried out the experiments and analyzed data.

References

1. Fan, T., Deser, C. & Schneider, D. P. Recent Antarctic sea ice trends in the context of Southern Ocean surface climate variations since 1950. *Geophys. Res. Lett.* **41**, 2419–2426 (2014).

2. Armour, K. C., Marshall, J., Scott, J. R., Donohoe, A. & Newsom, E. R. Southern Ocean warming delayed by circumpolar upwelling and equatorward transport. *Nat. Geosci.* **9**, 549–554 (2016).

3. Fogt, R. L., Raphael, M. N. & Handcock, M. S. Seasonal Antarctic Sea Ice Extent Reconstructions, 1905-2020, Version 1. [object Object] https://doi.org/10.7265/55X7-WE68 (2023).

4. Latif, M., Martin, T. & Park, W. Southern Ocean Sector Centennial Climate Variability and Recent Decadal Trends. *J. Clim.* **26**, 7767–7782 (2013).

5. Cabré, A., Marinov, I. & Gnanadesikan, A. Global Atmospheric Teleconnections and Multidecadal Climate Oscillations Driven by Southern Ocean Convection. *J. Clim.* **30**, 8107–8126 (2017).

6. Zhang, L., Delworth, T. L., Cooke, W. & Yang, X. Natural variability of Southern Ocean convection as a driver of observed climate trends. *Nat. Clim. Change* **9**, 59–65 (2019).

7. Hartmann, D. L. The Antarctic ozone hole and the pattern effect on climate sensitivity. *Proc. Natl. Acad. Sci.* **119**, e2207889119 (2022).

8. Heede, U. K. & Fedorov, A. V. Colder Eastern Equatorial Pacific and Stronger Walker Circulation in the Early 21st Century: Separating the Forced Response to Global Warming From Natural Variability. *Geophys. Res. Lett.* **50**, e2022GL101020 (2023).

9. Kang, S. M. *et al.* Global impacts of recent Southern Ocean cooling. *Proc. Natl. Acad. Sci.* **120**, e2300881120 (2023).

10. Wills, R. C. J., Dong, Y., Proistosecu, C., Armour, K. C. & Battisti, D. S. Systematic Climate Model Biases in the Large-Scale Patterns of Recent Sea-Surface Temperature and Sea-Level Pressure Change. *Geophys. Res. Lett.* **49**, e2022GL100011 (2022).

11. Zhang, X., Deser, C. & Sun, L. Is There a Tropical Response to Recent Observed Southern Ocean Cooling? *Geophys. Res. Lett.* **48**, e2020GL091235 (2021).

12. Dong, Y., Armour, K. C., Battisti, D. S. & Blanchard-Wrigglesworth, E. Two-way teleconnections between the Southern Ocean and the tropical Pacific via a dynamic feedback. *J. Clim.* **1**, 1–37 (2022).

13. Blanchard-Wrigglesworth, E., Roach, L. A., Donohoe, A. & Ding, Q. Impact of winds and Southern Ocean SSTs on Antarctic sea ice trends and variability. *J. Clim.* **1**, 1–47 (2020).

14. Hwang, Y.-T., Xie, S.-P., Deser, C. & Kang, S. M. Connecting tropical climate change with Southern Ocean heat uptake: Tropical Climate Change and SO Heat Uptake. *Geophys. Res. Lett.* **44**, 9449–9457 (2017).

15. Mechoso, C. R. *et al.* Can reducing the incoming energy flux over the Southern Ocean in a CGCM improve its simulation of tropical climate?: Southern Ocean-Tropics Link in a CGCM. *Geophys. Res. Lett.* **43**, 11,057-11,063 (2016).

16. Kang, S. M. *et al.* ETIN-MIP Extratropical-Tropical Interaction Model Intercomparison Project – Protocol and Initial Results. *Bull. Am. Meteorol. Soc.* (2019) doi:10.1175/BAMS-D-18-0301.1.

17. Stevens, B., Sherwood, S. C., Bony, S. & Webb, M. J. Prospects for narrowing bounds on Earth's equilibrium climate sensitivity. *Earths Future* **4**, 512–522 (2016).

18. Rugenstein, M., Zelinka, M., Karnauskas, K., Ceppi, P. & Andrews, T. Patterns of Surface Warming Matter for Climate Sensitivity. *Eos* **104**, (2023).

19. Zhou, C., Zelinka, M. D. & Klein, S. A. Impact of decadal cloud variations on the Earth's energy budget. *Nat. Geosci.* **9**, 871–874 (2016).

20. Andrews, T. *et al.* Accounting for Changing Temperature Patterns Increases Historical Estimates of Climate Sensitivity. *Geophys. Res. Lett.* **45**, 8490–8499 (2018).

21. Dong, Y. *et al.* Intermodel Spread in the Pattern Effect and Its Contribution to Climate Sensitivity in CMIP5 and CMIP6 Models. *J. Clim.* **33**, 7755–7775 (2020).

22. Kim, H., Kang, S. M., Kay, J. E. & Xie, S.-P. Subtropical clouds key to Southern Ocean teleconnections to the tropical Pacific. *Proc. Natl. Acad. Sci.* **119**, e2200514119 (2022).

23. Newman, M. *et al.* The Pacific Decadal Oscillation, Revisited. *J. Clim.* **29**, 4399–4427 (2016).

24. Henley, B. J. *et al.* A Tripole Index for the Interdecadal Pacific Oscillation. *Clim. Dyn.* **45**, 3077–3090 (2015).

25. Zhang, R. *et al.* A Review of the Role of the Atlantic Meridional Overturning Circulation in Atlantic Multidecadal Variability and Associated Climate Impacts. *Rev. Geophys.* **57**, 316–375 (2019).

26. Xie, S.-P. *et al.* Global Warming Pattern Formation: Sea Surface Temperature and Rainfall*. *J. Clim.* **23**, 966–986 (2010).

27. Wang, H., Xie, S.-P. & Liu, Q. Comparison of Climate Response to Anthropogenic Aerosol versus Greenhouse Gas Forcing: Distinct Patterns. *J. Clim.* **29**, 5175–5188 (2016).

28. Deser, C. *et al.* Isolating the Evolving Contributions of Anthropogenic Aerosols and Greenhouse Gases: A New CESM1 Large Ensemble Community Resource. *J. Clim.* **33**, 7835–7858 (2020).

29. Zebiak, S. E. Air–Sea Interaction in the Equatorial Atlantic Region. *J. Clim.* **6**, 1567–1586 (1993).

30. Jia, F. & Wu, L. A Study of Response of the Equatorial Pacific SST to Doubled-CO2 Forcing in the Coupled CAM–1.5-Layer Reduced-Gravity Ocean Model. *J. Phys. Oceanogr.* **43**, 1288–1300 (2013).

31. Qu, X., Hall, A., Klein, S. A. & DeAngelis, A. M. Positive tropical marine low-cloud cover feedback inferred from cloud-controlling factors. *Geophys. Res. Lett.* **42**, 7767–7775 (2015).

32. Klein, S. A., Hall, A., Norris, J. R. & Pincus, R. Low-Cloud Feedbacks from Cloud-Controlling Factors: A Review. *Surv. Geophys.* **38**, 1307–1329 (2017).

33. Bronselaer, B. *et al.* Change in future climate due to Antarctic meltwater. *Nature* **564**, 53–58 (2018).

34. Sadai, S., Condron, A., DeConto, R. & Pollard, D. Future climate response to Antarctic Ice Sheet melt caused by anthropogenic warming. *Sci. Adv.* **6**, eaaz1169 (2020).

35. Dong, Y., Pauling, A. G., Sadai, S. & Armour, K. C. Antarctic Ice-Sheet Meltwater Reduces Transient Warming and Climate Sensitivity Through the Sea-Surface Temperature Pattern Effect. *Geophys. Res. Lett.* **49**, e2022GL101249 (2022).

36. Smith, T. M., Reynolds, R. W., Peterson, T. C. & Lawrimore, J. Improvements to NOAA's Historical Merged Land–Ocean Surface Temperature Analysis (1880–2006). *J. Clim.* **21**, 2283–2296 (2008).

37. Kay, J. E. *et al.* The Community Earth System Model (CESM) Large Ensemble Project: A Community Resource for Studying Climate Change in the Presence of Internal Climate Variability. *Bull. Am. Meteorol. Soc.* **96**, 1333–1349 (2015).

38. Santer, B. D. *et al.* Statistical significance of trends and trend differences in layer-average atmospheric temperature time series. *J. Geophys. Res. Atmospheres* **105**, 7337–7356 (2000).

39. Schneider, D. P. & Deser, C. Tropically driven and externally forced patterns of Antarctic sea ice change: reconciling observed and modeled trends. *Clim. Dyn.* **50**, 4599–4618 (2018).

40. Peng, G., Meier, W. N., Scott, D. J. & Savoie, M. H. A long-term and reproducible passive microwave sea ice concentration data record for climate studies and monitoring. *Earth Syst. Sci. Data* **5**, 311–318 (2013).

Figure 1. Observed and simulated SST for the SO cooling period (1979–2013) and SO warming period (1949–1978). Time series of observed (a) global mean (black) and SO (blue), and (b) tropical southeast Pacific (green, region highlighted in Figure 1c–e) SST anomalies from ERSSTv3b. Thin lines show the annual-mean anomalies, while the thick lines show smoothed time series with 10-year running mean. Red shading indicates the SO warming period and blue shading indicates the SO cooling period. SST trend maps from ERSSTv3b (c–e), SOPACE ensemble mean (f–h), LENS ensemble mean (i–k), and SO-driven ([SOPACE]-[LENS], l–n). Left column is for the SO cooling period, middle column is for the SO warming period, and right column is the difference between two periods. Dashed lines indicate 50°S and 70°S. Regions with statistically significant trends at 95% level are stippled.

Figure 2. Observed and simulated trends of tropical SST and Antarctic sea ice. (a) Tropical southeast Pacific SST trends, (b) tropical South Atlantic SST trends, and (c) Antarctic sea ice extent (SIE) trends. Box and whiskers show the distribution of ensemble members from SOPACE (orange) and LENS (blue) in the SO cooling period, SO warming period, and difference between the two periods. The box extends from the first quartile to the third quartile, with the line showing median value. The whiskers extend from the box to the farthest data point lying within 1.5x the inter-quartile range from the box. Observed values are shown by the black horizontal lines, and reconstructed SIE trends are shown by magenta horizontal lines. Individual ensemble members are shown in dots. Bottom panels show the SO-driven response (green hatched bars) and observed unforced trends (black bars) of (d) tropical southeast Pacific SST, (e) tropical South Atlantic SST, and (f) Antarctic SIE. Reconstructed unforced SIE trends are shown in magenta bars.

Figure 3. Mixed-layer budget for SO-driven SST trends. Left column shows the SO cooling period, middle column shows the SO warming period, and right column shows SO cooling–warming difference. Simulated SST trends (a–c) are compared to the SST trends computed from the surface energy budget (d–f). Terms that dominate the contribution to the SST trends include (g–i) surface net shortwave flux F_{SW}^{t}, (j–l) wind-induced latent heat flux $LH^{t}{}_{W}$, and (m–o) ocean dynamics F_{O}^{t} as a residual. Latitudes of 20°S, 0°, 20°N and longitudes of 0°, 90°W, 180°, 90°E are shown in gray grids.

Figure 4. Observed and simulated Antarctic sea ice fraction trends. Left column shows the SO cooling period, middle column shows the SO warming period, and right column shows SO cooling–warming difference. (a) Observed trends, (b-d) SOPACE ensemble mean trends, (e-g) LENS ensemble mean trends, (h-j) SO-driven trends. Regions with statistically significant trends at 95% level are stippled.

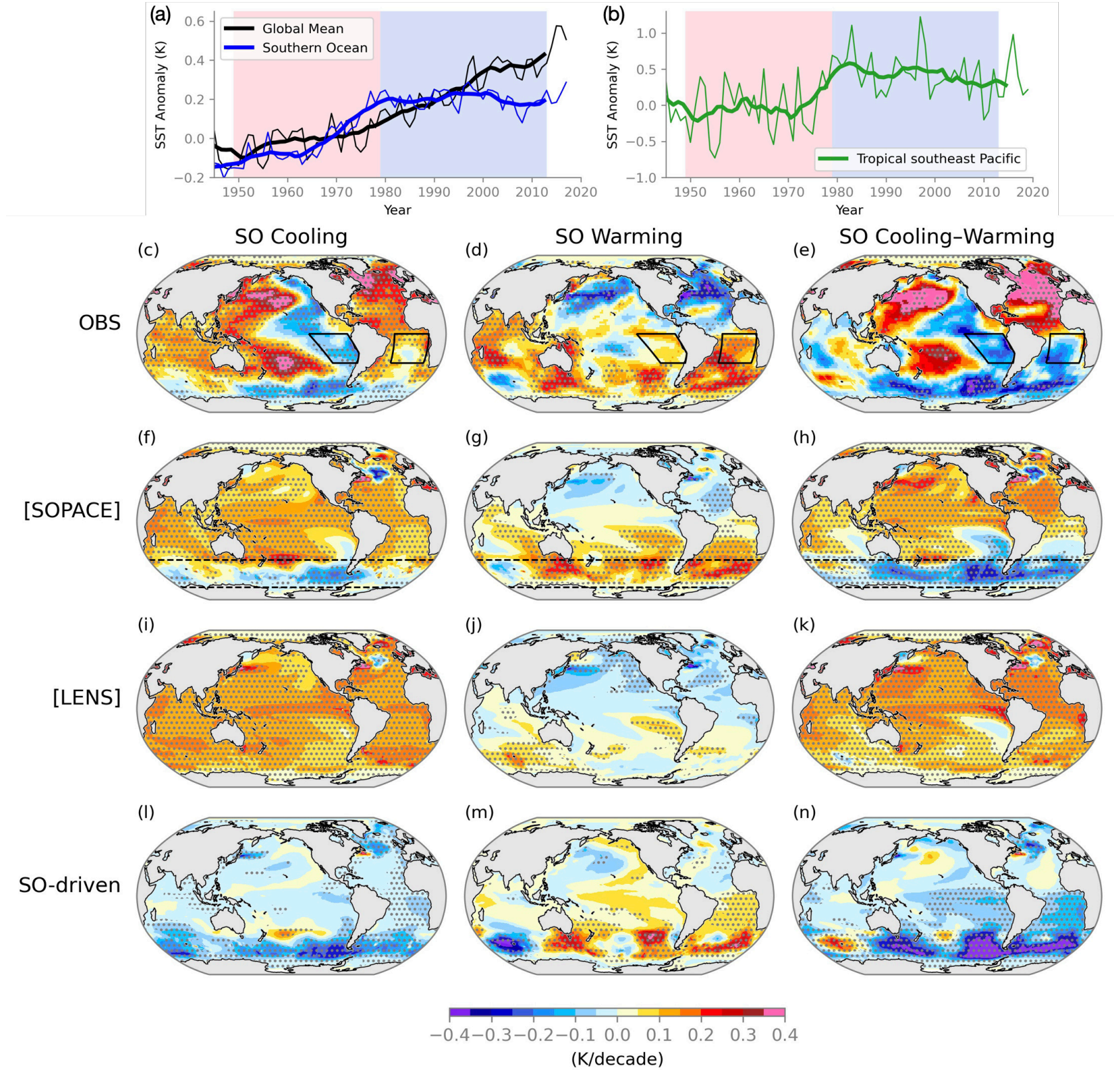
(a)
Global Mean
Southern Ocean
SST Anomaly (K)
Year
(b)
Tropical southeast Pacific
SST Anomaly (K)
Year
SO Cooling
SO Warming
SO Cooling–Warming
(c)
(d)
(e)
OBS
(f)
(g)
(h)
[SOPACE]
(i)
(j)
(k)
[LENS]
(l)
(m)
(n)
SO-driven
−0.4 −0.3 −0.2 −0.1 0.0 0.1 0.2 0.3 0.4
(K/decade)

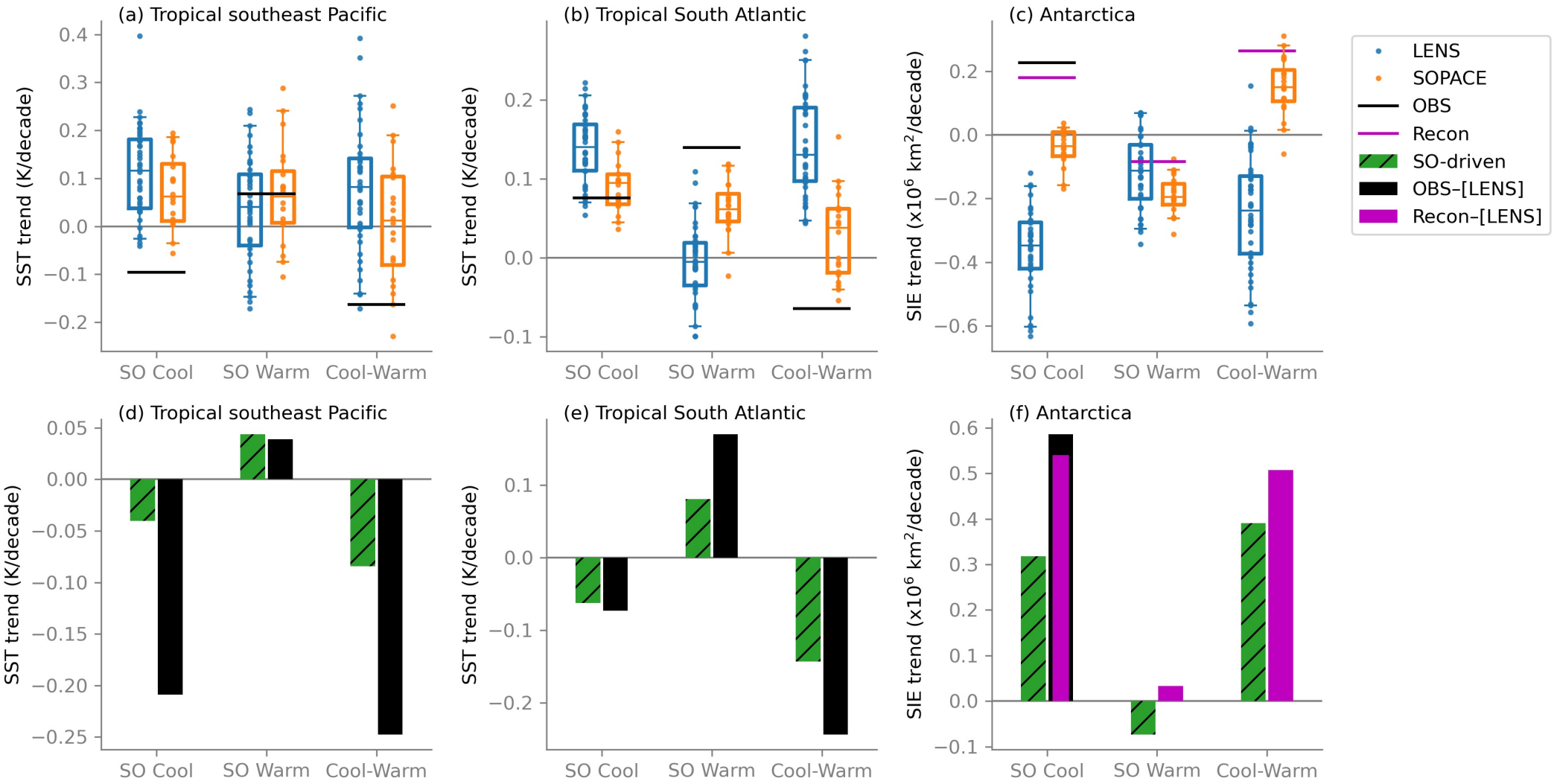
(a) Tropical southeast Pacific
(b) Tropical South Atlantic
(c) Antarctica
(d) Tropical southeast Pacific
(e) Tropical South Atlantic
(f) Antarctica
SST trend (K/decade)
SIE trend (x10^6 km^2/decade)
SO Cool
SO Warm
Cool-Warm
LENS
SOPACE
OBS
Recon
SO-driven
OBS–[LENS]
Recon–[LENS]

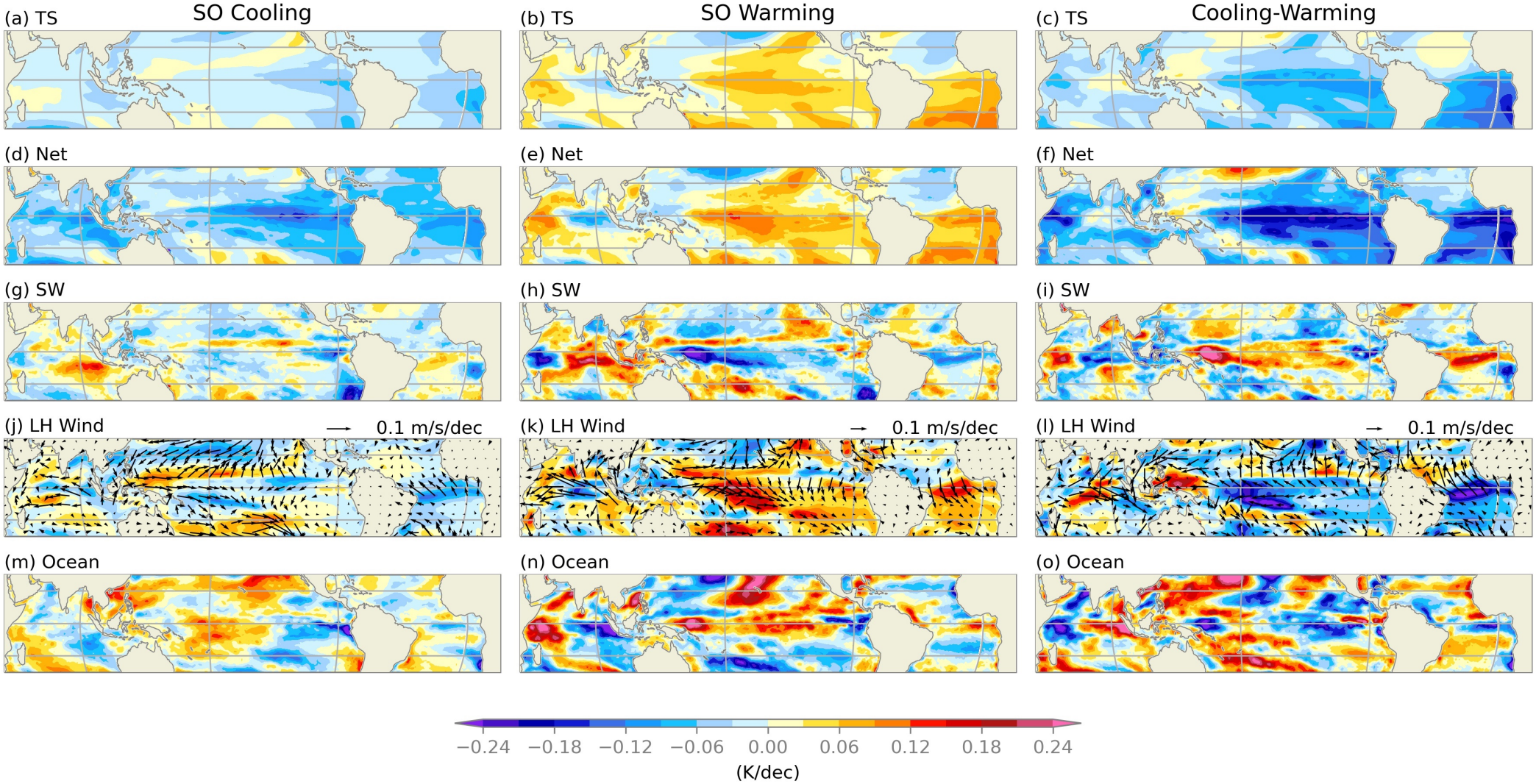
SO Cooling
SO Warming
Cooling-Warming
(a) TS
(b) TS
(c) TS
(d) Net
(e) Net
(f) Net
(g) SW
(h) SW
(i) SW
(j) LH Wind
0.1 m/s/dec
(k) LH Wind
0.1 m/s/dec
(l) LH Wind
0.1 m/s/dec
(m) Ocean
(n) Ocean
(o) Ocean
−0.24 −0.18 −0.12 −0.06 0.00 0.06 0.12 0.18 0.24
(K/dec)

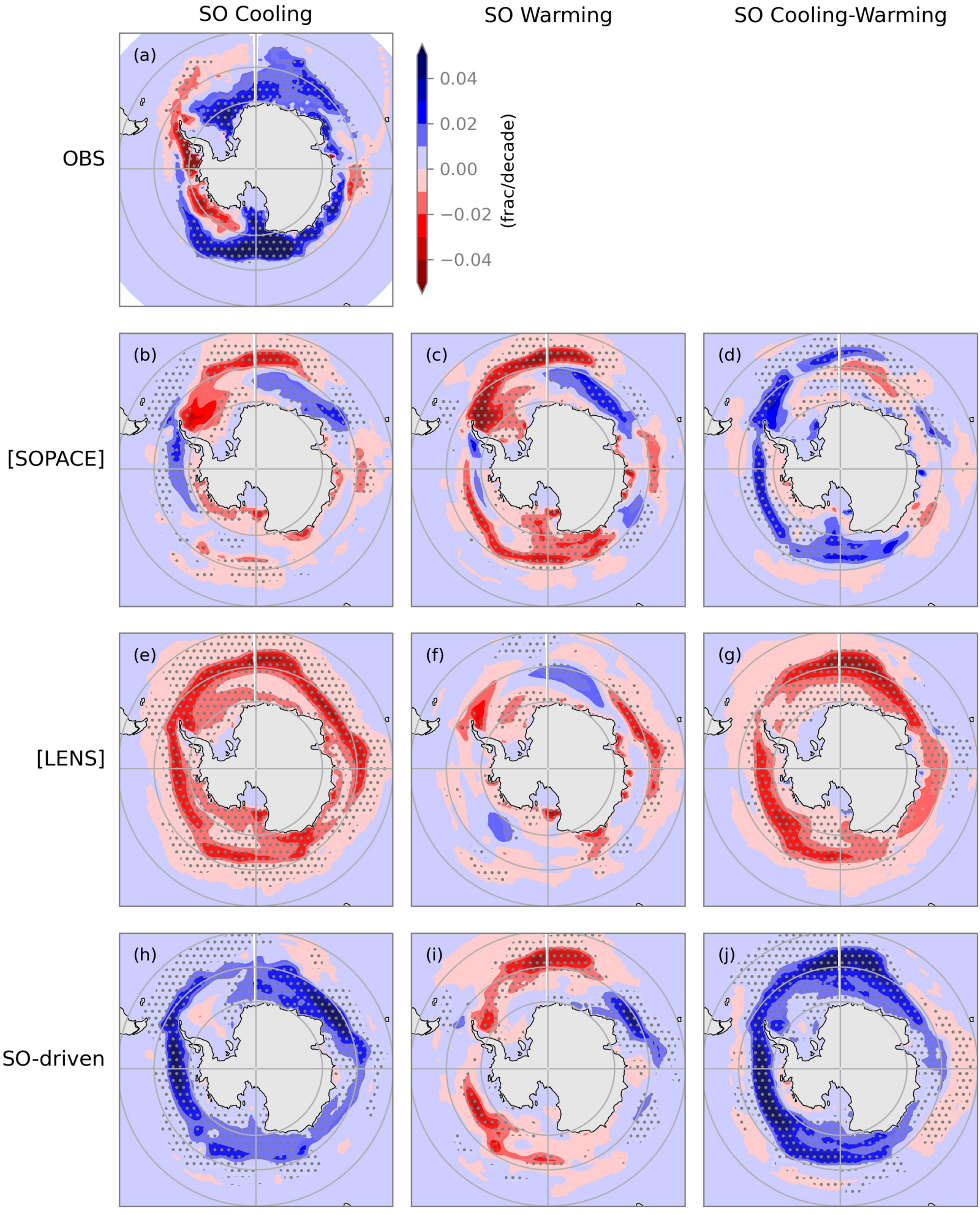
SO Cooling
SO Warming
SO Cooling-Warming
OBS
[SOPACE]
[LENS]
SO-driven
(a)
(b)
(c)
(d)
(e)
(f)
(g)
(h)
(i)
(j)
0.04
0.02
0.00
−0.02
−0.04
(frac/decade)